NASA/TM—2013-218069 GT2013–94695

Aerodynamic Measurements of a Variable-Speed Power-Turbine Blade Section in a Transonic Turbine Cascade at Low Inlet Turbulence

Ashlie B. Flegel-McVetta
Glenn Research Center, Cleveland, Ohio

Paul W. Giel
Vantage Partners LLC, Brook Park, Ohio

Gerard E. Welch
Glenn Research Center, Cleveland, Ohio

August 2013

NASA STI Program . . . in Profile

Since its founding, NASA has been dedicated to the advancement of aeronautics and space science. The NASA Scientific and Technical Information (STI) program plays a key part in helping NASA maintain this important role.

The NASA STI Program operates under the auspices of the Agency Chief Information Officer. It collects, organizes, provides for archiving, and disseminates NASA's STI. The NASA STI program provides access to the NASA Aeronautics and Space Database and its public interface, the NASA Technical Reports Server, thus providing one of the largest collections of aeronautical and space science STI in the world. Results are published in both non-NASA channels and by NASA in the NASA STI Report Series, which includes the following report types:

- TECHNICAL PUBLICATION. Reports of completed research or a major significant phase of research that present the results of NASA programs and include extensive data or theoretical analysis. Includes compilations of significant scientific and technical data and information deemed to be of continuing reference value. NASA counterpart of peer-reviewed formal professional papers but has less stringent limitations on manuscript length and extent of graphic presentations.

- TECHNICAL MEMORANDUM. Scientific and technical findings that are preliminary or of specialized interest, e.g., quick release reports, working papers, and bibliographies that contain minimal annotation. Does not contain extensive analysis.

- CONTRACTOR REPORT. Scientific and technical findings by NASA-sponsored contractors and grantees.

- CONFERENCE PUBLICATION. Collected papers from scientific and technical conferences, symposia, seminars, or other meetings sponsored or cosponsored by NASA.

- SPECIAL PUBLICATION. Scientific, technical, or historical information from NASA programs, projects, and missions, often concerned with subjects having substantial public interest.

- TECHNICAL TRANSLATION. English-language translations of foreign scientific and technical material pertinent to NASA's mission.

Specialized services also include creating custom thesauri, building customized databases, organizing and publishing research results.

For more information about the NASA STI program, see the following:

- Access the NASA STI program home page at *http://www.sti.nasa.gov*

- E-mail your question to *help@sti.nasa.gov*

- Fax your question to the NASA STI Information Desk at 443–757–5803

- Phone the NASA STI Information Desk at 443–757–5802

- Write to:
  STI Information Desk
  NASA Center for AeroSpace Information
  7115 Standard Drive
  Hanover, MD 21076–1320

NASA/TM—2013-218069 GT2013–94695

Aerodynamic Measurements of a Variable-Speed Power-Turbine Blade Section in a Transonic Turbine Cascade at Low Inlet Turbulence

Ashlie B. Flegel-McVetta
Glenn Research Center, Cleveland, Ohio

Paul W. Giel
Vantage Partners LLC, Brook Park, Ohio

Gerard E. Welch
Glenn Research Center, Cleveland, Ohio

Prepared for the
Turbo Expo 2013
sponsored by the American Society of Mechanical Engineers (ASME)
San Antonio, Texas, June 3–7, 2012

National Aeronautics and
Space Administration

Glenn Research Center
Cleveland, Ohio 44135

August 2013

Acknowledgments

This work is supported under the NASA Fundamental Aeronautics Program, Rotary Wing Project. The authors thank Adam Ford, Matt Bloxham, Steve Gegg, and Ed Turner of Rolls-Royce North American Technologies for their contributions during the blade design efforts under the RTAPS contract. The authors would also like to acknowledge the assistance of Doug Thurman (Army Research Laboratory) with acquiring hotwire measurements.

This work was sponsored by the Fundamental Aeronautics Program
at the NASA Glenn Research Center.

Level of Review: This material has been technically reviewed by technical management.

Available from

NASA Center for Aerospace Information
7115 Standard Drive
Hanover, MD 21076–1320

National Technical Information Service
5301 Shawnee Road
Alexandria, VA 22312

Available electronically at http://www.sti.nasa.gov

Aerodynamic Measurements of a Variable-Speed Power-Turbine Blade Section in a Transonic Turbine Cascade at Low Inlet Turbulence

Ashlie B. Flegel-McVetta
National Aeronautics and Space Administration
Glenn Research Center
Cleveland, Ohio 44135

Paul W. Giel
Vantage Partners, LLC
Brook Park, Ohio 44142

Gerard E. Welch
National Aeronautics and Space Administration
Glenn Research Center
Cleveland, Ohio 44135

Abstract

Aerodynamic measurements obtained in a transonic linear cascade were used to assess the impact of large incidence angle and Reynolds number variations on the 3-D flow field and midspan loss and turning of a 2-D section of a variable-speed power-turbine (VSPT) rotor blade. Steady-state data were obtained for ten incidence angles ranging from +15.8° to −51.0°. At each angle, data were acquired at five flow conditions with the exit Reynolds number (based on axial chord) varying over an order-of-magnitude from 2.12×10^5 to 2.12×10^6. Data were obtained at the design exit Mach number of 0.72 and at a reduced exit Mach number of 0.35 as required to achieve the lowest Reynolds number. Midspan total-pressure and exit flow angle data were acquired using a five-hole pitch/yaw probe surveyed on a plane located 7.0 percent axial-chord downstream of the blade trailing edge plane. The survey spanned three blade passages. Additionally, three-dimensional half-span flow fields were examined with additional probe survey data acquired at 26 span locations for two key incidence angles of +5.8° and −36.7°. Survey data near the endwall were acquired with a three-hole boundary-layer probe. The data were integrated to determine average exit total-pressure and flow angle as functions of incidence and flow conditions. The data set also includes blade static pressures measured on four spanwise planes and endwall static pressures. Tests were conducted in the NASA Glenn Transonic Turbine Blade Cascade Facility. The measurements reflect strong secondary flows associated with the high aerodynamic loading levels at large positive incidence angles and an increase in loss levels with decreasing Reynolds number. The secondary flows decrease with negative incidence as the blade becomes unloaded. Transitional flow is admitted in this low inlet turbulence dataset, making it a challenging CFD test case. The dataset will be used to advance understanding of the aerodynamic challenges associated with maintaining efficient power turbine operation over a wide shaft-speed range.

Introduction

A key goal of the Rotary Wing Project of the NASA Fundamental Aeronautics Program is the increased utilization of civil rotorcraft to relieve airport congestion and enhance airspace throughput capacity. The effort requires development/ maturation of technologies, including variable speed power turbines (VSPT, see D'Angelo (Ref. 1) and Welch (Ref. 2)), that enable economically competitive rotary-wing vehicles with both VTOL and Mach 0.5 cruise capability such as the Large Civil Tilt-Rotor (LCTR) concept vehicle (Johnson et al. (Ref. 3) and Acree et al. (Ref. 4)). Fuel burn is of prime importance and must be minimized by optimizing propulsive efficiency benefits achieved by slowing the main rotors at cruise through a VSPT shaft-speed change, while minimizing weight and SFC penalties associated with the variable-speed capability.

The key aerodynamic challenges of a VSPT include attainment of high turbine efficiency at high work factors, management of loss levels over a large (40° to 60°) incidence variation in all blade rows, and operation at low Reynolds numbers (transitional flow) (Welch (Ref. 2)). These challenges are derived by consideration of two key LCTR mission points: 2,000 ft takeoff/hover and 28,000 ft Mach 0.5 cruise. At takeoff, the main rotor and VSPT operate at 100 percent N^*, while at cruise the rotors and VSPT are slowed to 54 percent N^*. The LCTR engine requirements used herein were established with the NASA engine performance group (Ref. 5). The cruise and takeoff VSPT enthalpy extraction levels differ by only 8 to 10 percent. As the shaft is slowed from 100 to 54 percent N^* of takeoff speed, the turbine work factor ($\Delta h_o/U^2$) is increased by a factor of 3.4. The corrected flows (or Mach numbers) do not change significantly, and therefore the flow coefficient essentially doubles between the takeoff (100 percent) and cruise (54 percent) operating conditions. The nearly constant corrected flow rates and 40 percent corrected speed change lead to incidence angle

swings of 40° and 60° in all turbine blade and vane rows downstream of the first vane, including any required exit guide vane row. The unit Reynolds numbers (in^{-1}) at the aft-stage rotor exit of the VSPT for the LCTR application varies between $0.45\times10^5 < Re/C_x\ [in^{-1}] < 0.75\times10^5$ from takeoff to cruise. The impact of Reynolds number lapse on LPT bladerow performance is well documented in the literature (e.g., Hourmouziadis (Ref. 6), Haselbach (Ref. 7), Gier et al. (Ref. 8)), as is the sensitivity of the transitional flow fields to deterministic unsteadiness associated with upstream wakes (e.g., Halstead et al. (Ref. 9), and Coull et al. (Ref. 10)). The assessment of the impact of wake passing on blade row performance was beyond the scope of the present steady-state cascade study.

Several studies have been reported in the literature that address challenges relevant to variable-speed power turbines. Moustapha et al. (Ref. 11) have summarized previous work related to profile and secondary flow losses at design and off-design incidence conditions. Notably, Yamamoto and Nouse (Ref. 12) assessed the impact of incidence on the 3-D flow field and losses at five discrete setting angles spanning a range of incidence angles ($-53.3° < i < +7.2°$) of relevance to the present study. Their test was conducted in a low-speed linear cascade. Five-hole pitot probe surveys were obtained at 15 chordwise planes (hub to midspan) in a high turning (107°) turbine blade row. The chordwise development of the secondary flows and total-pressure fields were provided for the five incidence angles tested. The cross-passage contours illustrated pressure-side separation at extreme negative incidence angles. Similarly, the impact of incidence on blade loading was assessed using tip-endwall static pressure taps. The loading diagrams illustrated regions of negative loading, spanning increasing fractions of chord at increasingly extreme negative incidence angles.

In addition to Moustapha et al.'s (Ref. 11) valuable review of available cascade data with wide range of incidence angle testing, they noted that blade rows with high inlet Mach numbers would likely be more sensitive to inlet gas angle changes. They also noted the lack of data in the open literature related to the impact of compressibility, leading edge geometry, and axial loading schedule on incidence losses. Joinini et al. (Ref. 13) examined the impact of leading edge geometry—in particular, metal angle selection—on midspan incidence loss. They noted that detailed experimental data for off-design incidence, particularly in transonic flow conditions, were sparse in the open literature, and highlighted the importance of such data for CFD validation.

Hoheisel et al. (Ref. 14) measured 2-D profile loss as a function of incidence on front- and aft-loaded blading. The aft-loaded blading performed better in terms of loss at the different incidence levels at Tu = 5 percent. The most front-loaded blade performed more poorly at positive incidence but retained lower loss levels at negative incidence. Corriveau and Sjolander (Ref. 15) provided midspan profile losses, loading distribution, and base pressure measurements for a series of HPT airfoils with front-, mid-, and aft-loading. The linear cascade tests were conducted over a wide range of LPT-relevant Mach numbers and at Reynolds numbers from 0.4 to 1.0×10^6. While the results illustrated superior loss performance for aft-loaded blades, lower loss levels were achieved at off-design incidence with the mid-loaded blading.

The objective of the present study is to advance the understanding of the aerodynamic effects of large incidence angle and Reynolds number variations in order to address key VSPT challenges. The NASA Transonic Linear Cascade Facility, with its adjustable inlet flow angle test section (77° range) and wide range of flow capabilities, was used to assess the performance of a VSPT blade section at design and off-design inlet flow angles over an engine-relevant range of Mach and Reynolds numbers. The large-scale blades enabled detailed flow field measurements. Testing in the steady-state, non-rotating cascade inherently neglects the rotational effects associated with Coriolis and centrifugal acceleration fields, the relative motion of endwalls, and the impact of unsteadiness of upstream and downstream blade rows; nonetheless, a transonic cascade test of a VSPT blade section was deemed to be an appropriate step towards VSPT technology level advancement.

In the present study, detailed half-span flowfield measurements were acquired on a plane 7 percent axial-chord downstream of the blade trailing edge plane covering three blades passages. The measurements included total pressures and exit pitch and yaw angles which were acquired at the baseline flow condition for the LCTR-relevant takeoff (i = −36.7°) and cruise (i = +5.8°) points. Pitchwise integrated averages of these quantities were calculated as well. Endwall static pressures and blade loading data were also acquired at ten inlet angles and five flow conditions each. Midspan total pressure and exit pitch angle data were acquired for all flow angles and flow conditions. Averaged midspan total pressures were used to establish profile loss buckets. By admitting flow transition, the low turbulence data serves as a challenging test case for CFD code and model improvement.

Nomenclature

Cp_s	static pressure coefficient, $Cp_s = \left(P - \overline{P}_2\right)/\left(P_{t,1} - \overline{P}_2\right)$
Cp_t	total-pressure coefficient, $Cp_t = \left(P_{t,1} - P_t\right)/\left(P_{t,1} - \overline{P}_2\right)$
C_x	blade axial chord [in]
h_o	enthalpy
H	blade span [in]
i	incidence angle, $i = \beta_1$ – inlet metal angle (34.2°)
M	Mach number
N	power-turbine shaft speed [rpm]
N^*	$N/N_{100\%}$, fraction of 100 percent speed
PR	pressure ratio, $PR = P_{t,1}/\overline{P}_2$
PS	pressure surface

$\overline{P}$ 7 area-averaged static-pressure

$\overline{P_t}$ area-averaged total-pressure

Re Reynolds number, $Re = \rho U C_x / \mu$

Re_b baseline Reynolds number, $Re_b = 5.30 \times 10^5$

S blade pitch [in]

SS suction surface

Tu turbulence intensity, $Tu = \sqrt{u_s^2 + u_z^2} \,/ U$

U total mean velocity

$\underline{U}$ mean velocity [ft/s], $\underline{U} = (U_x, U_y, U_z)$

$\underline{u}$ fluctuating velocity, $\underline{u} = (u_x, u_y, u_z)$

x chordwise (axial) coordinate [in]

y pitchwise (tangential) coordinate [in]

z spanwise coordinate [in]

Zw Zweifel coefficient, $Zw = \dfrac{2S}{C_x} \cos^2 \overline{\beta}_2 (\tan \beta_1 - \tan \overline{\beta}_2)$

β relative flow angle, pitch angle [deg.], $\beta = \tan^{-1}(U_y/U_x)$

$\overline{\beta}_2$ angle of mass-averaged velocity components

$\Delta\beta_2$ departure angle from trailing edge mean camber line

γ yaw angle [deg.], $\gamma = \tan^{-1}(U_z / U_x)$

δ_{99} boundary layer thickness [in.]

μ dynamic viscosity

ρ density

τ probe time constant [s]

ω loss coefficient, $\omega = \left(P_{t,1} - \overline{P}_t\right) / \left(P_{t,1} - \overline{P}_2\right)$

ω_c loss coefficient, $\omega_c = \omega \, (Re/Re_b)^{1/2}$

Subscripts

1 cascade inlet value

2 cascade exit value

i isentropic value

s streamwise component

t total condition

Description of Experiment

Facility Description

The aerodynamic assessment of the 2-D VSPT blade section was conducted in the NASA Glenn Research Center (GRC) Transonic Turbine Blade Cascade Facility shown in Figure 1. Verhoff et al. (Ref. 16) gave an initial facility description. Since then, two major facility modifications were made. The first modification, described by Giel et al. (Ref. 17), was made to improve the inlet flow uniformity. Recently, the exhaust duct was replaced and modifications were made to the structural supports in the test section in order to accommodate the inlet angle variation required for the current tests. Details of those modifications were given by McVetta et al. (Ref. 18).

The cascade's large scale and continuous run capability at engine relevant Mach numbers and Reynolds numbers have allowed for detailed aerodynamic (Refs. 18 and 19) and heat transfer studies (Refs. 20 and 20) on a wide range of turbine blades.

The cascade's operating envelope is illustrated in Figure 2. Inlet air is supplied by GRC's 40 psig combustion air system. Clean, dry, ambient temperature air enters the facility and is throttled to a maximum inlet pressure of 14.7 psia under current safety restrictions. This restriction is shown as the red dashed line in Figure 2. The air passes through flow conditioning and contraction sections and is directed to the cascade test section by upper and lower flow boards. The air is then exhausted through an altitude exhaust system that is maintained at 2 psia.

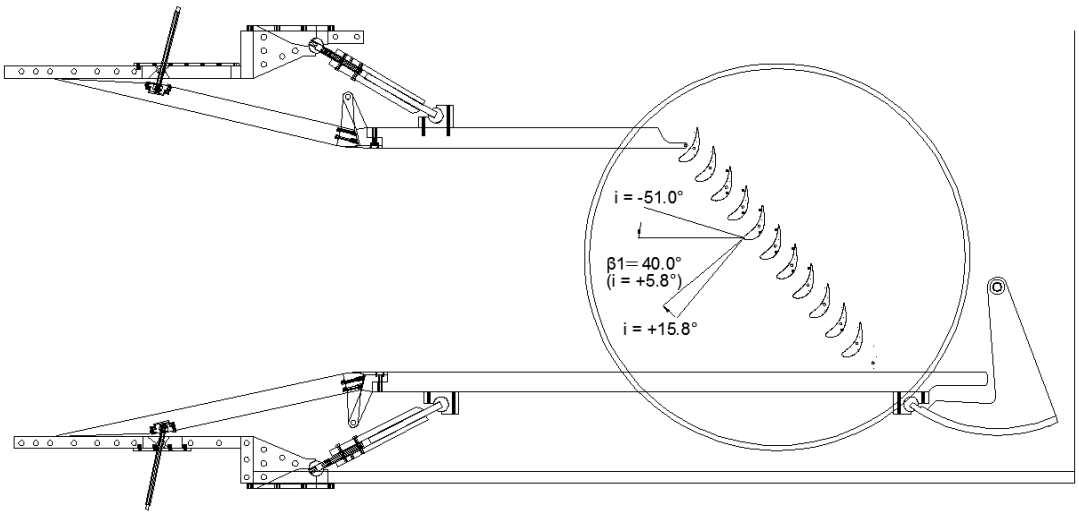

Figure 1.—Cascade Test Section with Blade Geometry.

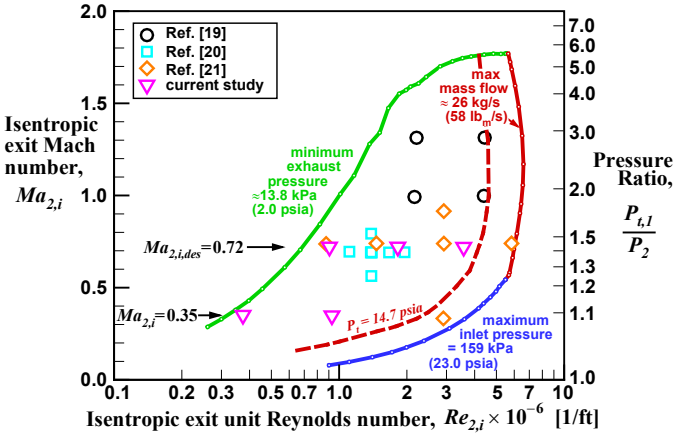

Figure 2.—Operating Envelope of NASA Transonic Turbine Cascade.

The cascade for this test was made up of nominally ten blade passages. The blades are attached to a disk that can be rotated to set inlet flow angles (from axial) in the range $-17° \le \beta_1 \le +78.8°$. This allows for a wide range of incidence angles to be studied. Ten incidence angles were tested as listed in Table 1. More detailed data were acquired at incidence angles of +5.8° and −36.7°, which represent the cruise and takeoff flight mission points, respectively. Unique upper flow board extensions with respective blade suction-side profiling were fabricated for five discrete incidence angles in the range of $-16.1° \le i \le -51.0°$. For these five angles, the upper-most blade was removed and replaced with a flow board extension that bolted to the end of the upper flow board and to the upper blade bolt-hole location. These extensions ensured that the flow was properly directed into the first blade passage, the upper and lower flow boards were horizontal, and their hinged leading edges were maintained in the same plane normal to the inlet flow.

At each incidence angle setting, data were acquired at the five nominal flow conditions listed in Table 2. The design pressure ratio was 1.412 which corresponds to an exit isentropic Mach number of 0.72. A baseline flow condition was established by finding the lowest Reynolds number at which the tunnel could consistently maintain an exit Mach number of 0.72. The baseline Reynolds number, Re_b, was found to be 0.53×10^6. Higher Reynolds number cases were run at 1.06×10^6 and 2.12×10^6. An order-of-magnitude variation in Reynolds number could be achieved by reducing the exit Mach number to 0.35. The lowest Reynolds number point of 2.12×10^5 could not be achieved at the design exit Mach number due to the limitations of the tunnel operating envelope (see Figure 2).

The inlet boundary-layer thickness range is documented for each flow condition in Table 2. The boundary-layer heights were calculated by inlet Reynolds number scaling (turbulent flow) of detailed inlet boundary-layer measurements acquired in a previous study (Ref. 19). The range in Table 2 indicates the variation in the boundary-layer thickness for the ten incidence angles and corresponding inlet Reynolds number variations.

TABLE 1.—ANGLES SETTINGS AND ZWEIFEL COEFFICIENTS

Inlet angle, β_1	Incidence angle, i	Zw
50.0°	15.8°	1.22
45.0°	10.8°	1.13
40.0° (Cruise)	5.8°	1.06
34.2°	0.0°	0.99
28.0°	−6.2°	0.92
18.1°	−16.1°	0.82
8.2°	−26.0°	0.74
−2.5° (Takeoff)	−36.7°	0.65
−11.8° (Mission Max-i)	−46.0°	0.58
−16.8°	−51.0°	0.53

TABLE 2.—NOMINAL FLOW CONDITIONS

Exit Re_{Cx}	Pressure ratio	Exit, M_{is}	$\delta_{99,1}$,[a] in.	$2\delta_{99,1}/H$ [a]
2.12×10^6	1.412	0.72	1.16 to 1.23	0.39 to 0.41
1.06×10^6	1.412	0.72	1.28 to 1.36	0.43 to 0.45
5.30×10^5	1.412	0.72	1.42 to 1.50	0.47 to 0.50
5.30×10^5	1.087	0.35	1.40 to 1.49	0.47 to 0.50
2.12×10^5	1.087	0.35	1.60 to 1.69	0.53 to 0.56

[a] Reynolds-scaling estimated range of boundary-layer thickness over ten incidence angle settings.

The facility has an optional upstream blowing turbulence grid located roughly five axial-chords upstream of the blade row. Hoheisel et al. (Ref. 14) described the influence of turbulence intensity on the location of 2-D transition and on trailing edge suction-side momentum thickness for the suction surface of front- and aft-loaded blading. The transition point moved upstream with increasing Tu and appeared always to be associated with a laminar separation bubble. At low turbulence intensities (Tu = 0.8 percent), the trailing edge momentum thickness increased monotonically with diffusion level. Since the minimum accessible tunnel exit Reynolds number (0.53×10^6) at $M_{2,i}$= 0.72 of the present effort was significantly higher than that anticipated for engine cruise (e.g., 0.045×10^6 – 0.15×10^6) it was decided to test without the turbulence grid (i.e., at low turbulence) in order to admit transitional flow appropriate to altitude conditions. A planned follow-on tunnel entry includes testing at higher turbulence intensities (Tu = 7 to 8 percent). In a previous study (Ref. 18) the inlet turbulence intensity without a grid was documented to range from 0.25 to 0.40 percent. The integral length scale was found to be 25 mm (1.0 in.) to 38 mm (1.5 in.) which is largely independent of Reynolds number and immersion in the boundary layer. The integral length scale was found though an autocorrelation technique (e.g., see Coull et al. (Ref. 22)).

Blade Description

The blade geometry is a scaled 2-D midspan section of the VSPT second stage rotor shown in Figure 3. Details of the blade design are documented in (Ref. 23). In that effort,

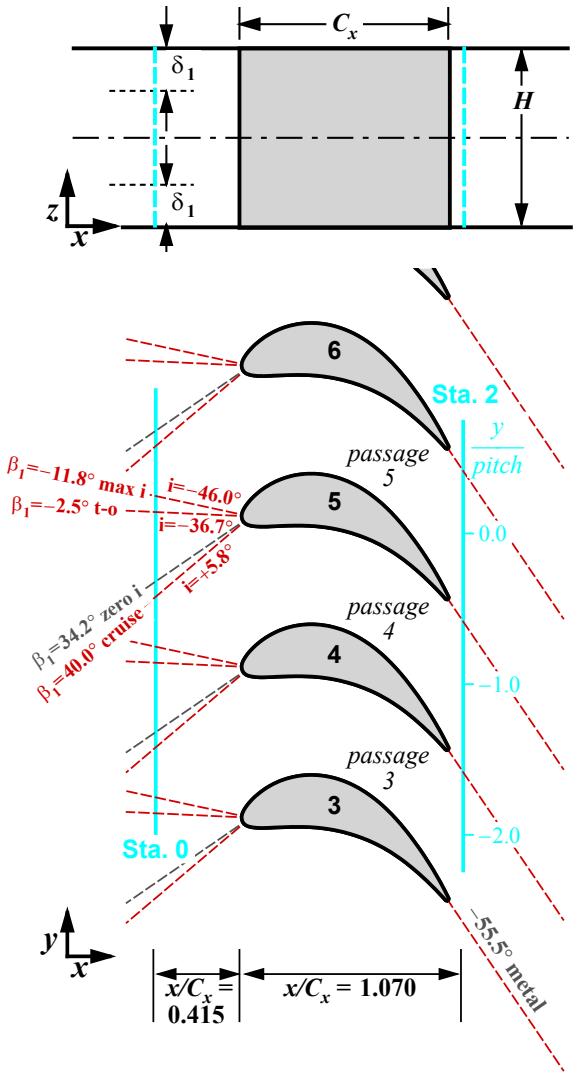

Figure 3.—Blade Geometry and Survey Plane Location.

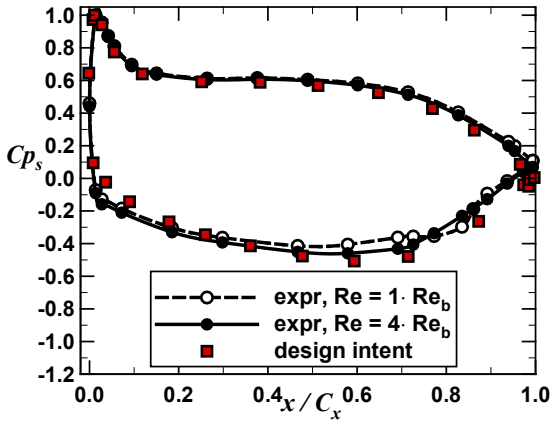

Figure 4.—Design Intent and Experimental Data at High and Low Reynolds Numbers and Design Exit Mach Number at i = +5.8°.

TABLE 3.—BLADE DESCRIPTION

Geometry	Value
Axial chord, C_x, mm (in.)	180.57 (7.109)
True chord, mm (in.)	194.44 (7.655)
Pitch, S, mm (in.)	130.00 (5.119)
Span, H, mm (in.)	152.40 (6.000)
Throat diameter, mm (in.)	72.85 (2.868)
Leading edge diameter, mm (in.)	15.16 (0.597)
Trailing edge diameter, mm (in.)	3.30 (0.130)
Stagger angle	20.35°
Inlet metal angle	34.2°
Uncovered turning	19.47°
Exit metal angle	−55.54°

meanline analyses were used to analyze three and four-stage variable-speed power turbines (VSPT) to meet specified engine requirements. After considering stage efficiency potential versus work factor (e.g., Smith Chart, Smith (Ref. 24)), which restricts the level of acceptable stage work factor, a four-stage turbine was selected. A detailed 3-D blade aero design/optimization was concentrated on the second rotor of the selected four-stage meanline design. Rotor 2 was selected as a representative embedded blade row, both in terms of turning (96° at cruise and 53° at takeoff) and incidence-range (42°) requirements between cruise and takeoff (Ref. 23). The midspan section, which was optimized to minimize loss at the cruise condition (i = +5.8°, $M_{2,i}$ = 0.72) and achieve required incidence range at acceptable loss levels, was chosen for this cascade test. The blade has an inlet metal angle of 34.2° relative to the axial direction and a scaled axial chord of 180.6 mm (7.109 in.). Details of the scaled (test) blade are listed in Table 3. Again, the cascade of the current test comprised ten blade passages (nominally).

The design blade loading diagram (Ref. 23) compared to the experimental midspan data at two Reynolds number conditions is shown in Figure 4. The design calculation (reproduced from (Ref. 23)) was carried out in 2-D on a cone assuming fully turbulent flow whereas the midspan of the experiment is influenced by the strong three-dimensionality and secondary flow fields in the low aspect ratio cascade (see Figure 3) and transitional flow effects. The optimum profile from the design is considered to be aft-loaded and has notably high uncovered turning (19.5°) with respect to the suction-surface curvature.

Description of Measurements

Total-pressure and exit flow angle data were obtained using a five-hole pitch-yaw probe and a three-hole boundary-layer probe. Both are 45° forward-facing pyramid probes with the measurement port located on the shaft centerline. The probes are similar with the exception of the three-hole probe's flattened measurement head. The probes were installed in the Station 2 survey plane located approximately 7.0 percent axial-chord

downstream of the blade trailing edge as shown in Figure 3. The five-hole probe measures total-pressure, pitch angle (*x*-*y* plane), and yaw angle (*x*-*z* plane). For each inlet angle, the five-hole probe was used for midspan surveys consisting of 123 pitchwise points spaced non-uniformly over the three passages noted in Figure 3. Pitchwise/spanwise surveys were also taken at the takeoff and cruise incidence angles. The surveys at each immersion consisted of 62 pitchwise points spaced uniformly over three passages. The three-hole boundary-layer probe measured total pressure and pitch angle only and could be traversed to touch the endwall, at which point its measurement port center was located approximately 0.13 mm (0.005 in.) from the endwall surface. The three-hole probe was used near the endwall for $0.0 < z/H \leq 0.043$ with 14 spanwise points spaced logarithmically. The five-hole probe was used above this region for $0.042 \leq z/H \leq 0.50$ with 12 spanwise points spaced uniformly. Detailed probe descriptions and calibration methods were provided in Giel et al. (Ref. 19). The time responses for each probe were measured to be: $\tau_{5\text{-hole}} = 0.42$ s and $\tau_{3\text{-hole}} = 0.82$ s. To ensure a 95 percent time recovery, a three second delay was imposed between the time the probe reaches the desired survey location and the data recording. The probe pitch angle coefficient was monitored to ensure that it remained within the angular calibration range of ±40°. When needed, the probe survey was stopped and the probe was approximately nulled before resuming. The overall estimated uncertainty in flow angle was ±1.5° and the overall estimated local uncertainty in total-pressure coefficient was ±0.8 percent, as reported in Giel et al. (Ref. 19) and scaled for the current definition of total-pressure coefficient.

The primary measurements blades 4, 5, and 6, shown in Figure 3, were instrumented with static pressure taps at four spanwise locations. Blade 5 was fully instrumented with 44 taps along 10, 15, 30, and 50 percent of span. A pre-test RANS prediction of the blade surface pressure distribution was used to establish the placement of the blade 5 static taps. To verify periodicity, 20 redundant taps were installed on the suction side of blade 4 and 16 taps were installed on the pressure side of blade 6.

The endwall was fully instrumented with static pressure taps located both upstream and downstream of the blade row and within each passage. Data from these pressure measurements were used for periodicity checks. In Figure 5, data from the endwall pressure taps located near the Station 2 survey plane ($x/C_x = 1.070$) are shown for two inlet angles for the baseline Reynolds number and design exit Mach number condition. These data are also compared to the blade base pressures measured on blades 4, 5, and 6. The pressures are influenced by the downstream exhaust configuration that induces a pitchwise static pressure nonuniformity which is shown in Figure 5; the aperiodicity is negligible at positive incidence angles, but increases at the negative incidence angle settings. This aperiodicity will be observable in the flowfield data discussed later.

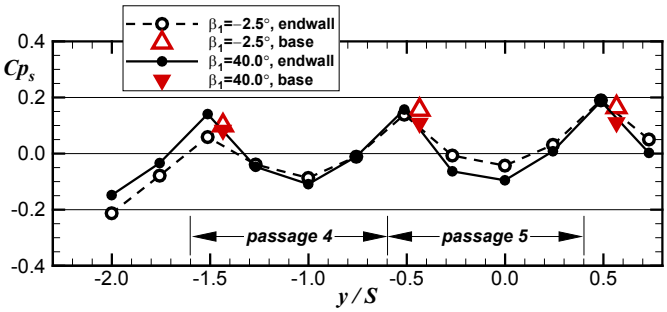

Figure 5.—Station 2 Endwall and Midspan Blade Base Pressures at $Re_{Cx} = 5.30\times10^5$ (Re_b) and $M_{2,i} = 0.72$.

Twelve exit static-pressure taps, located approximately three axial-chords downstream of the blades and spanning almost nine blade pitches, were used to set the exit Mach number condition. The inlet static pressure was measured by five to six inlet static pressure taps, depending on inlet flow angle, located 96.77 mm (3.81 in.) upstream of the blade row at Station 0. Inlet total pressure and temperature were measured with two combination Kiel/total-temperature probes also located at midspan approximately 96.77 mm (3.81 in.) upstream of the blades, just outside the passages of interest.

Experimental Results

3-D Flowfield Results at $Re_{Cx,2} = 1 \cdot Re_b$

Survey Data

Detailed flowfield surveys were obtained at 26 spanwise locations for incidence angles of $i = -36.7°$ ($\beta_1 = -2.5°$, takeoff) and $i = +5.8°$ ($\beta_1 = 40.0°$, cruise) at the baseline Reynolds number (Re_b) and nominal design exit Mach number ($M_{2,i} = 0.72$). The total-pressure contours in Figure 6 reflect that the blade is highly loaded at the positive incidence cruise condition (Figure 6(a)), producing strong secondary flows which drive the endwall flow to and along the suction side of the blade. As the incidence angle decreases to $i = -36.7°$ (Figure 6(b)), blade loading is reduced and a largely two-dimensional exit total pressure is measured (cf. Yamamoto and Nouse (Ref. 12)).

The secondary-flow vectors and pitch and yaw flow angles over one blade passage are shown in Figure 7 and Figure 8 for both the positive and negative incidence angles. The impact of strong secondary flows is evident at the highly loaded $i = +5.8°$ condition. In Figure 7, the high negative pitch angles near the endwall ($z = 0$), reflect strong overturning near the hub. The pitch and yaw angles in Figure 7(b) and (c) reflect the secondary-flow induced passage vortex. The core of the horseshoe vortex, located approximately at $y/S = -0.45$ and $z/H = 0.33$, is evident in the crossflow vectors as well. At $i = -36.7°$, little pitch and yaw angle variation is observed due to the two dimensionality of the flowfield.

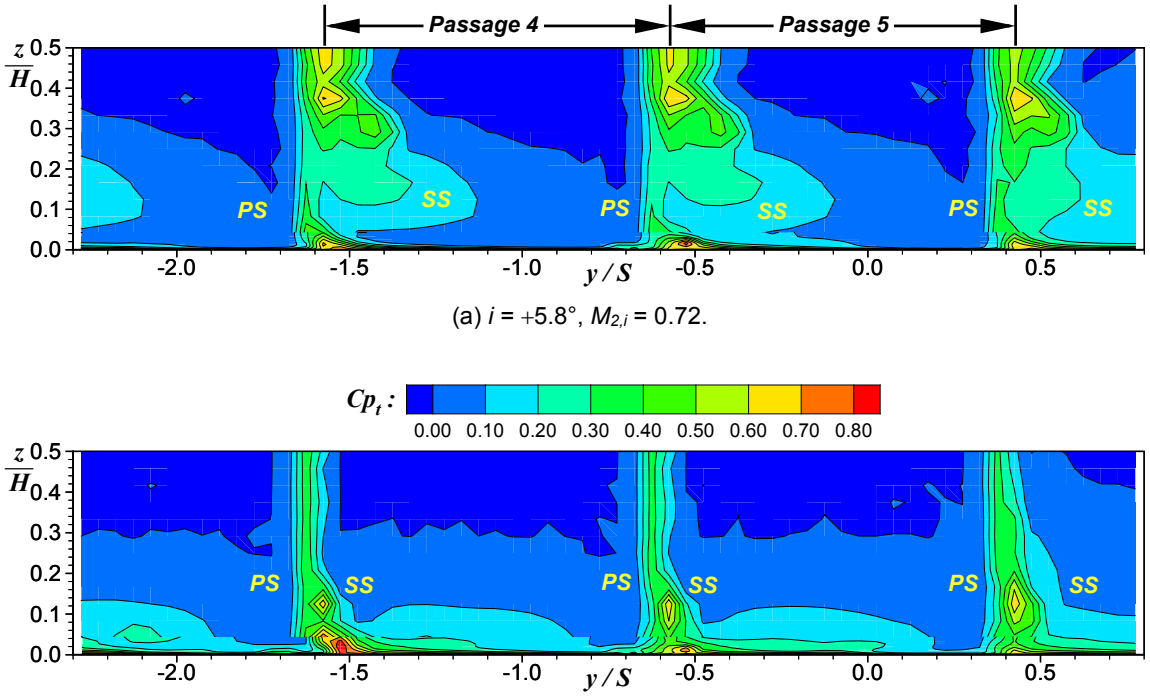

(a) i = +5.8°, $M_{2,i}$ = 0.72.

(b) i = –36.7°, $M_{2,i}$ = 0.67.

Figure 6.—Total Pressure Coefficient Contours at $Re_{Cx,2} = Re_b$ Over Three Passages.

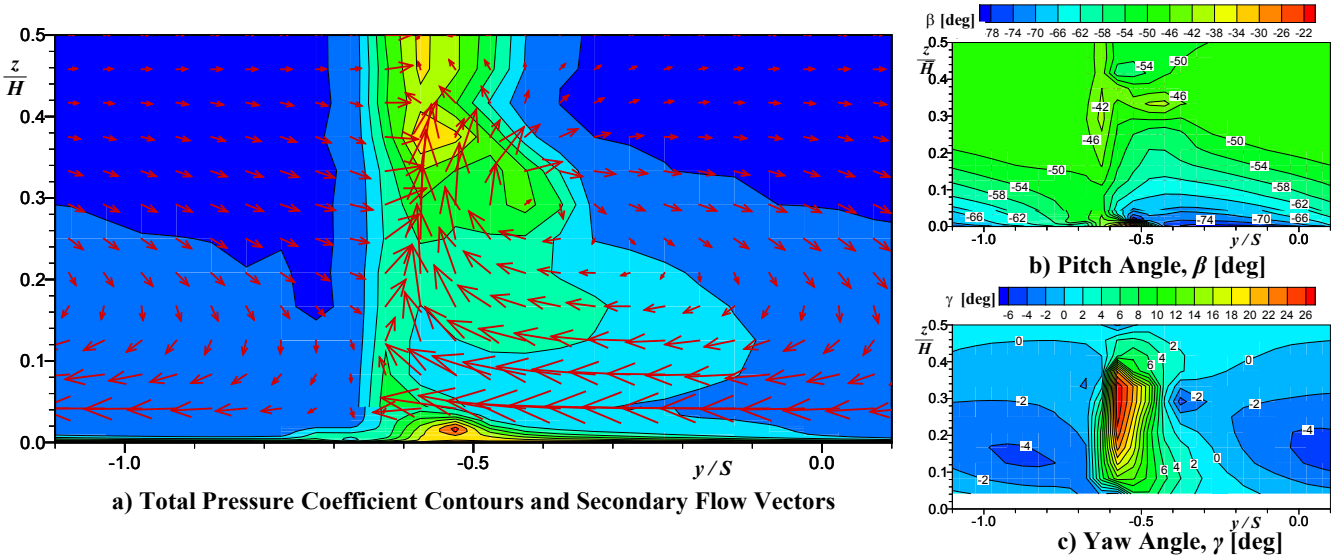

Figure 7.—Detailed View of Flow at i = +5.8°, $Re_{Cx,2}$ = 5.30×10^5 (Re_b), $M_{2,i}$ = 0.72.

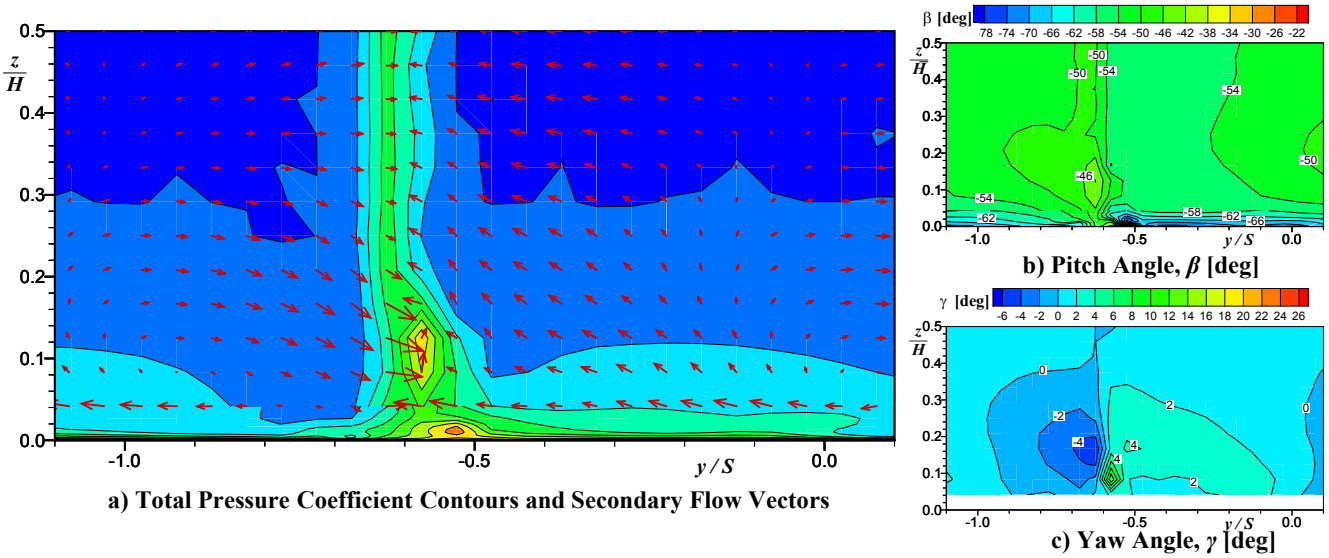

Figure 8.—Detailed View of Flow at i = −36.7°, $Re_{Cx,2}$ = 5.30×10^5 (Re_b), $M_{2,i}$ = 0.67.

The total-pressure and pitch angle data of the three- and five-hole probe measurements were in good agreement at both incidence angles as seen at z/H = 0.042. The agreement was evident in the integrated averages (shown later). For all the flowfield data presented there is reasonable periodicity between passages four and five. Passage six exhibits a slight aperiodicity, which is consistent with the endwall data shown in Figure 5.

Pitchwise Integrations

Pitchwise integrations of the total-pressure coefficient, pitch angle, and yaw angle were calculated at each spanwise immersion for i = +5.8° (Figure 9) and i = −36.7° (Figure 10). The area-averaged total-pressure coefficient (Figure 9(a) and (b)) reflects strong spanwise variation in the secondary-flow field; the thick inlet boundary-layer fluid is thinned out near the hub and transported to a higher span section on the blade suction side. Area-averaging of the total pressure was performed so that calculated loss coefficients would account for loss production both within the blade passage and in downstream mixing. The estimated inlet boundary layer, noted in Table 3, for this flow condition is 1.44 in., which accounts for roughly 24 percent of the blade span. As seen in the flowfield contours (Figure 6 to Figure 8), the horseshoe vortex and its core location can be seen in Figure 9(c) and (d) at z/H = 0.33. The pitch angle in Figure 9(c) show the flow is always overturned near the hub. The point of minimum turning is located at z/H = 0.33. This is the same spanwise location of the maximum yaw angle shown in Figure 9(d).

The integrations at i = −36.7° are shown in Figure 10. The inlet boundary-layer thickness was 1.50 in., roughly 50 percent of the half-span; due to the two-dimensionality of the flow at this incidence angle, the boundary-layer thickness at the exit remains nearly consistent through the blades. The pitch angle in Figure 10(c) reflects overturning at the endwall; further up the span, the flow tends towards the exit metal angle and remains constant spanwise.

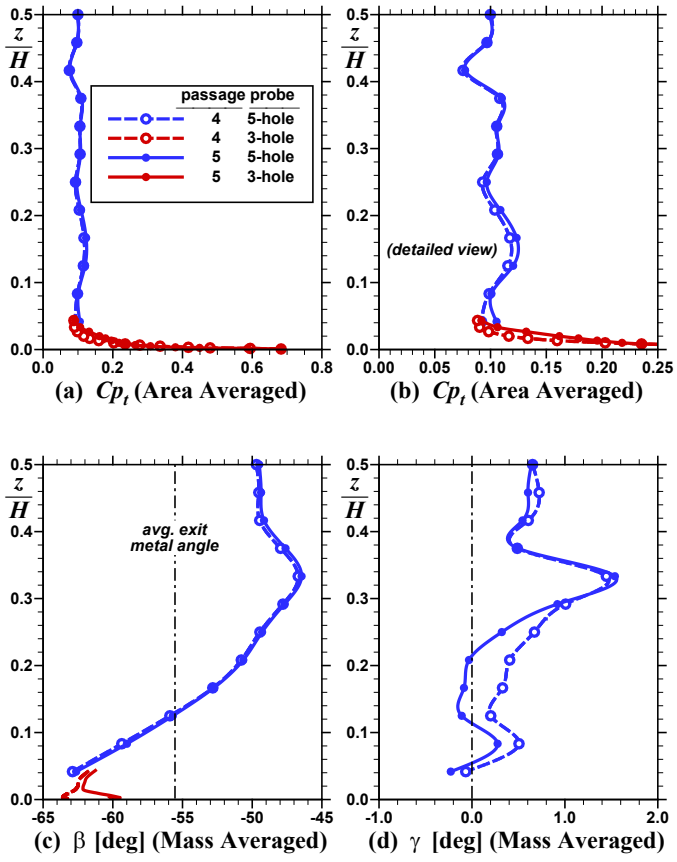

Figure 9.—Pitchwise Integrations for i = +5.8°.

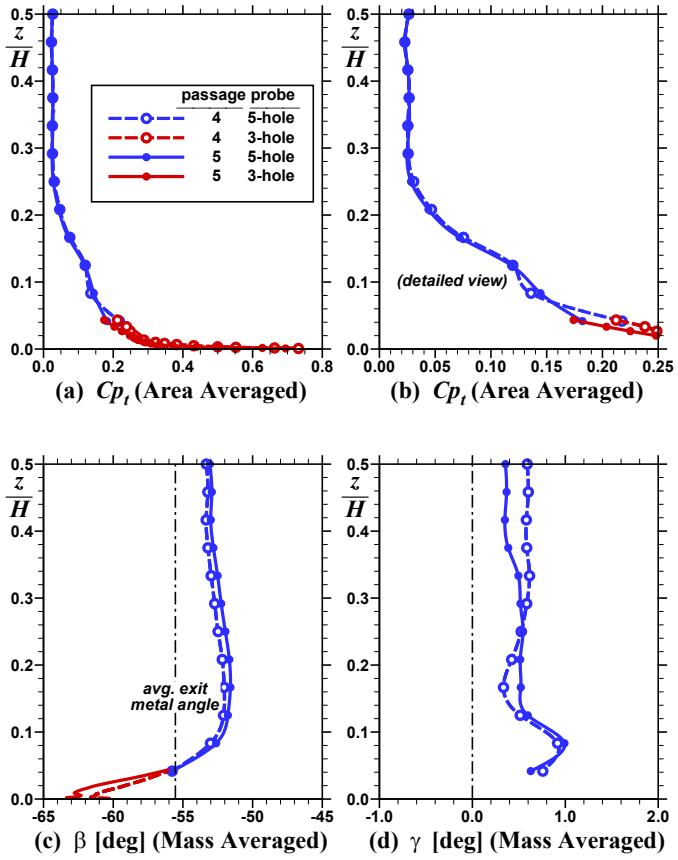

Figure 10.—Pitchwise Integrations for i = −36.7°.

The total-pressure integrations for both angles show good agreement between each passage and between the three-hole and five-hole probes. The yaw angle data could only be acquired with the five-hole probe. Passage-to-passage differences in measured yaw angles, and the average offset from 0°, are within the measurement uncertainty.

Blade Loading

The effects of incidence and Reynolds number on blade loading are shown in Figure 11. All data in this figure were acquired at the nominal design exit Mach number ($M_{2,i}$ = 0.72) with the exception of i = −36.7° and −51.0° at which maximum exit Mach numbers of 0.67 and 0.62 could be obtained, respectively, due to facility limitations. The plots are arranged with the highest Reynolds number on the left ((a) to (e), 4·Re_b) and the baseline Reynolds number on the right (f) to (j), 1·Re_b). The entire range of tested incidence angles is presented.

At the highest positive incidence, Figure 11(a) and (f), the high blade loading results in highly three-dimensional flow as evidenced by the spanwise loading variations. This is consistent with the flowfield data shown in Figure 6 for the positive incidence case. Despite the spanwise loading

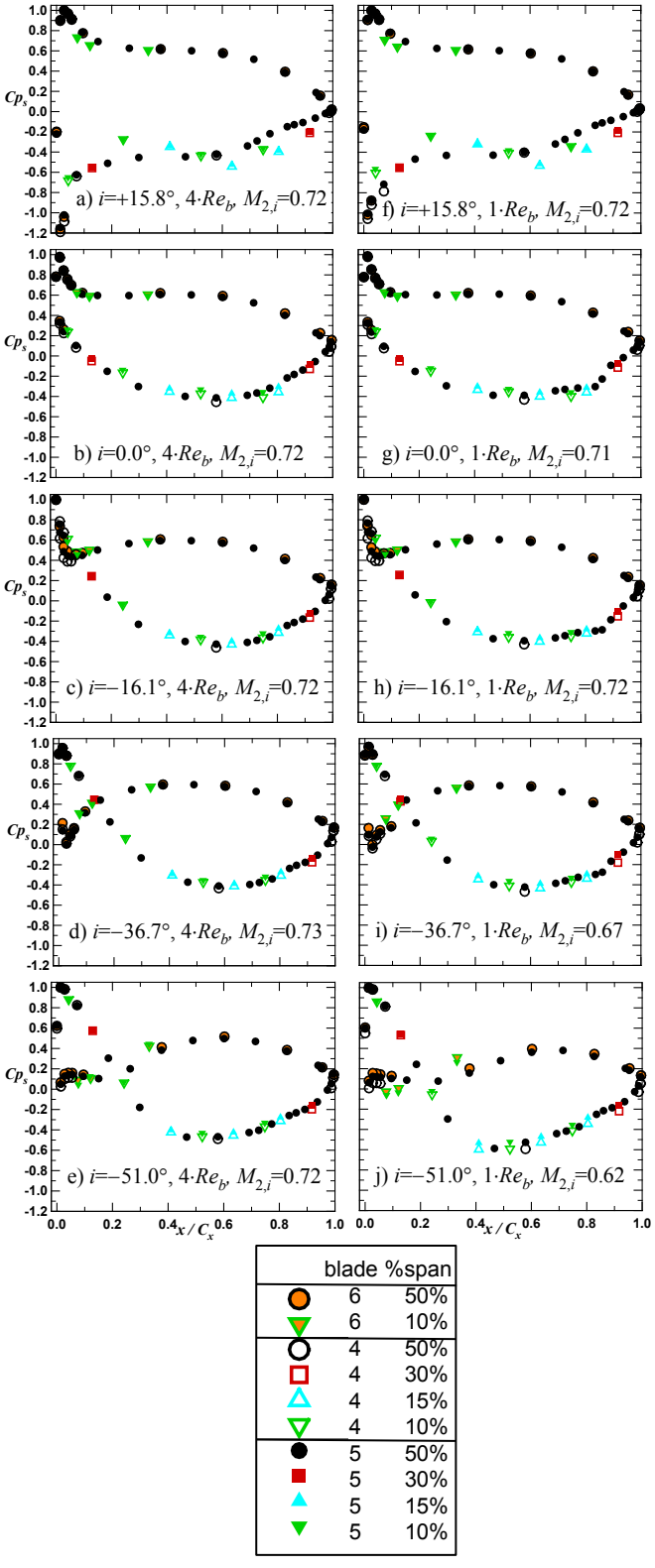

Figure 11.—Blade Loading—Effects of Incidence and Reynolds Number at Nominal Design Exit Mach Number.

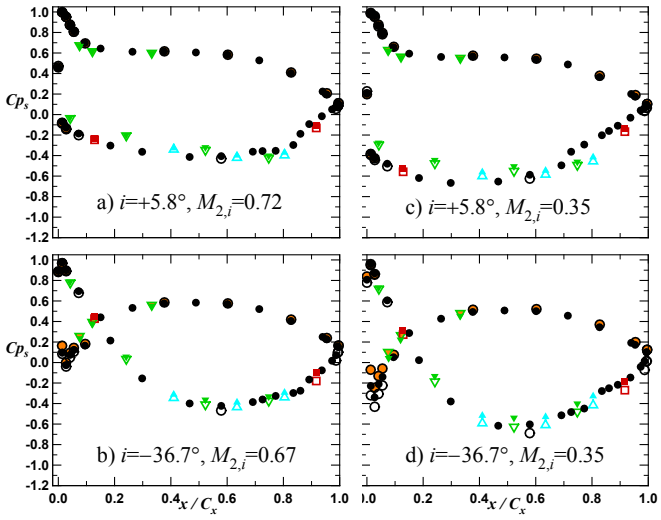

Figure 12.—Blade Loading—Effects of Exit Mach Number at $Re_{Cx,2}$ = 5.30×10^5 (Re_b).

variations, the data show excellent periodicity. As incidence decreases, the front portions of the blades unload and the flow becomes increasingly two-dimensional. For $i < -16.1°$, negative loading is measured at the front portion of the blades and at the extreme negative incidence angles (i = −51.0°) a pressure-side cove separation is observed and is reflected in the midspan exit surveys shown later. This is consistent with Yamamoto and Nouse (Ref. 12) and Brear et al. (Ref. 25).

For the baseline Reynolds number cases shown in Figure 11(f) to (j), the suction surface exhibits a neutral pressure gradient region, followed by an abrupt diffusion. This jump is indicative of a reattachment following a laminar separation bubble (see Hoheisel et al. (Ref. 14)). For i = –51.0°, the reattachment occurs relatively early at $x/C_x \approx 0.45$. For i = –36.7°, –16.1°, and 0.0°, it occurs farther aft on the suction surface at $0.83 \le x/C_x \le 0.87$. For i = +15.8°, reattachment occurs near $x/C_x \approx 0.59$.

The effects of exit Mach number on blade loading are shown in Figure 12. All data in this figure were acquired at the baseline Reynolds number. The loading increases and the location of minimum Cp_s moves forward with decreasing $M_{2,i}$. The increased diffusion causes the suction-surface reattachment points to move forward.

2-D Midspan Results

Exit Survey Data

The effects of Reynolds number and Mach number variations on the midspan total-pressure and exit flow angle (pitch angle) surveys are presented in Figure 13 to Figure 15. These surveys consisted of 123 points concentrated in the wakes over the three passages. At a high positive incidence angle of +10.8° (Figure 13), the blade row is highly loaded

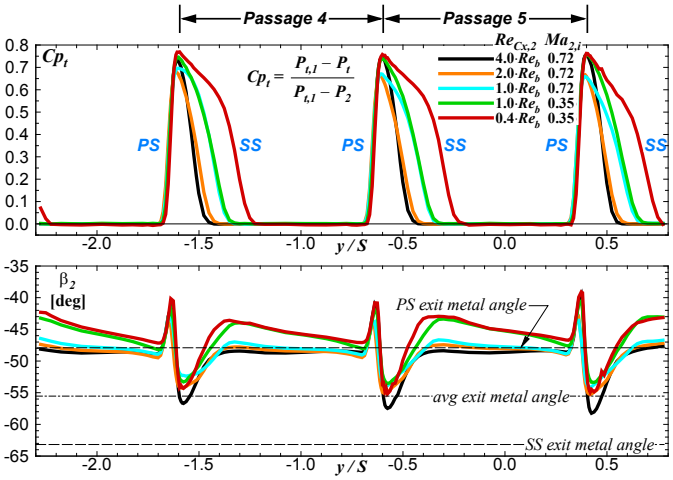

Figure 13.—Effects of Reynolds Number and Exit Mach Number at i = +10.8°.

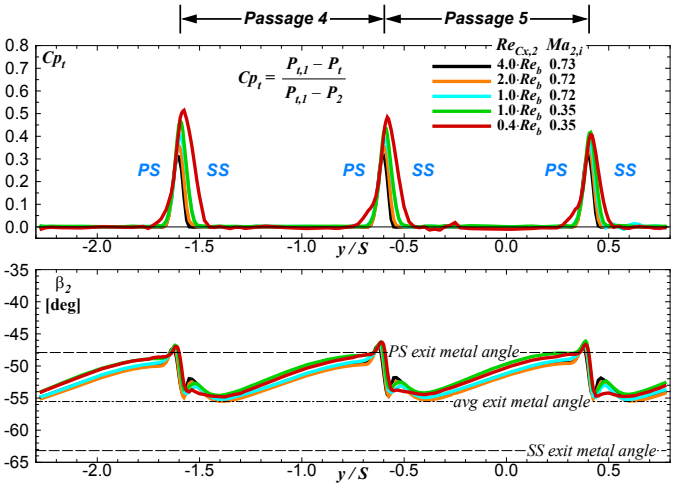

Figure 14.—Effects of Reynolds Number and Exit Mach Number at i = −36.7°.

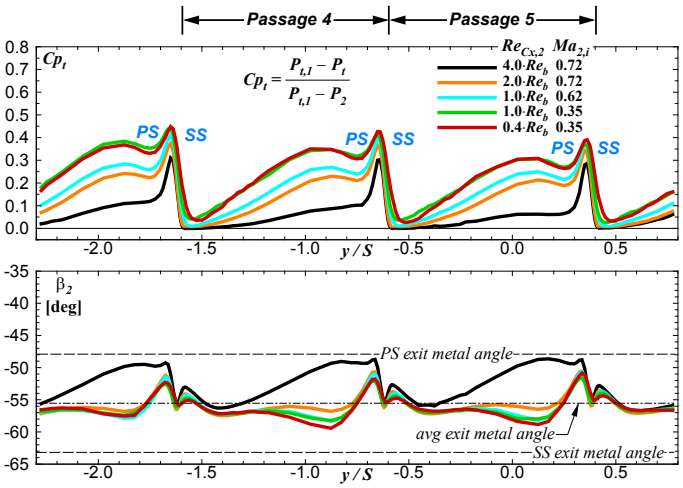

Figure 15.—Effects of Reynolds Number and Exit Mach Number at i = −51.0°.

and the exit surveys are consistent with the two-dimensional suction-side separation at midspan noted in the blade loading diagrams. The separation and resultant wake thickening, seen in the total-pressure wake profile (top), increases with decreasing Reynolds number. At the baseline Reynolds number, $1{\cdot}Re_b$, the wake widths remain constant as the exit Mach number is varied from 0.72 (design) to 0.34. The measured exit flow angles reflect that the flow turning is relatively independent of Reynolds number variation and decreases as the Mach number is reduced. Similar trends in the total-pressure and exit flow angle data were observed as positive incidence levels were reduced. As expected, suction-side wake widths decreased as the loading and incidence angles were reduced.

As noted in the three-dimensional flowfield measurements, as the incidence angle is reduced, the blade loading and secondary-flow driven three-dimensionality of the flow field decreases. The corresponding midspan measurements taken at the −36.7° incidence angle are shown in Figure 14. The overall levels of Cp_t have decreased at this condition. Minimal suction-side thickening was measured even at the lowest Reynolds and Mach number condition. Note that, at this incidence angle, a small amount of pressure-side thickening was observed at the $M_{2,i}$ = 0.35 and $Re_{Cx,2}$ = 2.12×10^5 flow condition. The exit flow angle shows little variation with changing Reynolds number and only varies between the pressure-side exit metal angle and the average exit metal angle.

The results for the largest negative incidence, i = −51.0°, tested are provided in Figure 15. A pressure-side separation wake extends over the majority of the blade pitch. As the Reynolds number decreases, the wake thickness on the suction-side increases slightly while the wake depth and thickness on the pressure side increases dramatically. The pressure-side wake is reflective of a massive pressure-side separation with associated aerodynamic blockage. At this angle, it is also noted that the wake profile remains unchanged at the fixed Mach number ($M_{2,i}$ = 0.35) condition as Reynolds number is varied from $1{\cdot}Re_b$ to $0.4{\cdot}Re_b$. The exit flow angle varies little with Reynolds number and remains near the average exit metal angle, except for the highest Reynolds number ($4{\cdot}Re_b$) condition which has lower exit flow angle. The exit flow angle for the $4{\cdot}Re_b$ condition is consistent with the angles seen in Figure 14, where there is minimal pressure-side separation. The exit angles and loss profiles indicate that at the extreme negative incidence conditions, as Reynolds number is decreased, the pressure-side separation-induced wake thickens substantially. The increased aerodynamic blockage on the pressure-side resets the aerodynamic throat upstream and effects increased turning and a more negative discharge angle.

The effects of incidence-angle variation at the highest and lowest Mach number and Reynolds number conditions are summarized in Figure 16 and Figure 17, respectively; an order-of-magnitude variation in Reynolds number is reflected across these figures. The three incidence angles correspond to cruise (i=+5.8°), takeoff (i=−36.7°), and maximum mission incidence (i=−46.0°). At the highest Reynolds number ($4{\cdot}Re_b$) in Figure 16, the positive incidence produces an overall higher loss that decreases with decreasing incidence and loading. Large variations with incidence are observed in Figure 17 at the lowest Reynolds number ($0.4{\cdot}Re_b$), and an exit Mach number of 0.35. At the positive incidence angle, consistent with the blade loading in Figure 11, there is strong indication of an extensive separation on the suction side. As the incidence decreases, the blade is unloaded and the losses decrease. At i = −36.7°, the suction-side is attached and a slight increase in pressure-side losses are observed. As the negative incidence increases further, there is evidence of extensive pressure-side separation.

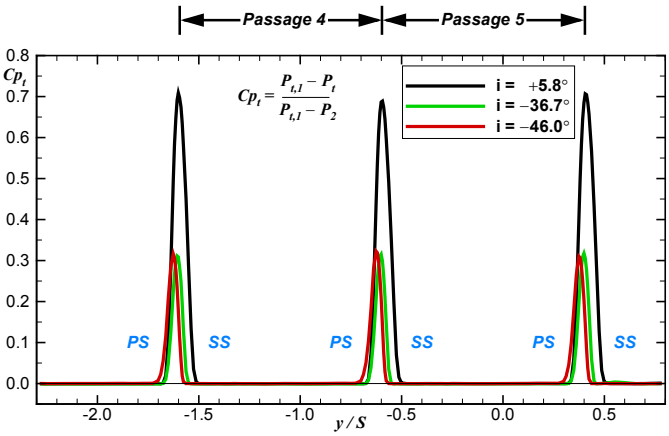

Figure 16.—Effect of Incidence Angle at $Re_{Cx,2}$= 2.12 × 10^6 ($4{\cdot}Re_b$) and $Ma_{i,2}$ = 0.72.

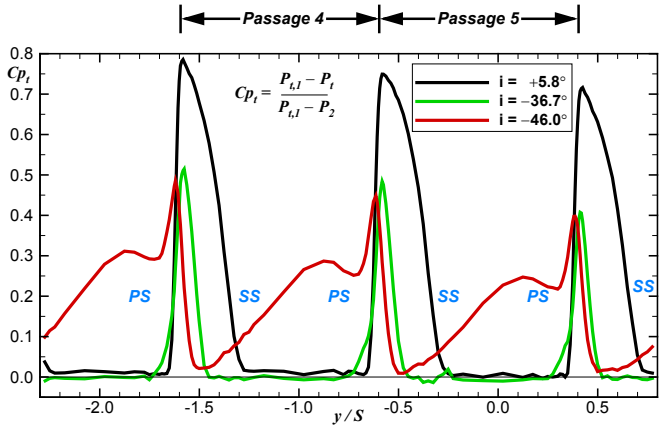

Figure 17.—Effect of Incidence Angle at $Re_{Cx,2}$= 2.12 × 10^5 ($0.4{\cdot}Re_b$) and $Ma_{i,2}$ = 0.347.

Midspan Loss Coefficients

Area-averaged integrations of the total-pressure data were used to calculate midspan profile loss coefficients, ω, for each incidence angle and flow condition. Midspan loss coefficients are plotted as a function of incidence in Figure 18. The integrations were calculated separately over two complete Passages, 4 and 5. Passage-to-passage variations are noted at the extreme negative incidence angles. As expected, as the Reynolds number decreases, loss levels increase and the loss bucket narrows. For the two conditions where the baseline Reynolds number (Re_b) is held constant and the Mach number is varied from $M_{2,i}$ = 0.72 to $M_{2,i}$ = 0.35, the loss levels are independent of Mach number except at the extreme positive (i = +15.8°) and negative (i = −46.0°, and −51.0°) incidence angles.

The midspan profile loss levels were plotted as a function of Reynolds number. The power-law functionality was examined and found to be indicative of regions of transitional flow, with the higher Reynolds numbers scaling with a −0.1 to −0.2 exponent (turbulent) and the lower Reynolds number scaling with −0.5 exponent (laminar); however, the power-law exponent was found to vary with incidence angle. Nonetheless, it is interesting that the strongest collapse of the overall bucket on Reynolds number, shown in Figure 19, was obtained with a $\omega \propto Re^{-0.5}$ scaling, indicative of a significant influence of laminar flow on the midspan loss levels.

The same loss data (Figure 18) were plotted in terms of reduced loss and incidence according to the Ainley-Mathieson (A-M) scaling (ω/ω_s versus i/i_s) (Ref. 26), shown in Figure 20. For each loss curve, $\omega_s = 2\times\omega_{i=0}$ and the stalling incidence, i_s, is the incidence corresponding to ω_s. The A-M scaling strongly collapses the data. Thus a canonical shape can be used to represent the data, with the following caveat: the narrowing of the loss bucket is found to be a function of Reynolds number to an extent beyond that tared out by the scaling on the stalling incidence. That is, the lack of collapse at the extreme negative incidence range, though consistent in Reynolds number, reflects a rate of change that is not tarred out by change in stalling incidence with Reynolds number.

Midspan Turning

The deviation angle, or the difference between the exit flow angle and the mean exit metal angle ($\Delta\beta_2 = \beta_2 + 55.54°$), is plotted as a function of incidence in Figure 21. Deviation angles asymptotically (see $i \geq -26.0°$) approached $\Delta\beta_2 = 2°$ as the blade unloads at the design Mach numbers ($M_{2,i}$ = 0.72) and $\Delta\beta_2 = 4°$ at the lower $M_{2,i}$ = 0.35 conditions. Deviation angles at cruise, i = +5.8°, are between $\Delta\beta_2 = 5°$ ($M_{2,i}$ = 0.72) and $\Delta\beta_2 = 9°$ ($M_{2,i}$ = 0.35). At the lower Reynolds number and extreme negative incidence angles, the exit flow angles shifts to the exit metal angle. The increased aerodynamic blockage on the pressure side of the airfoil, at reduced Reynolds numbers, is thought to effect the more negative discharge angle.

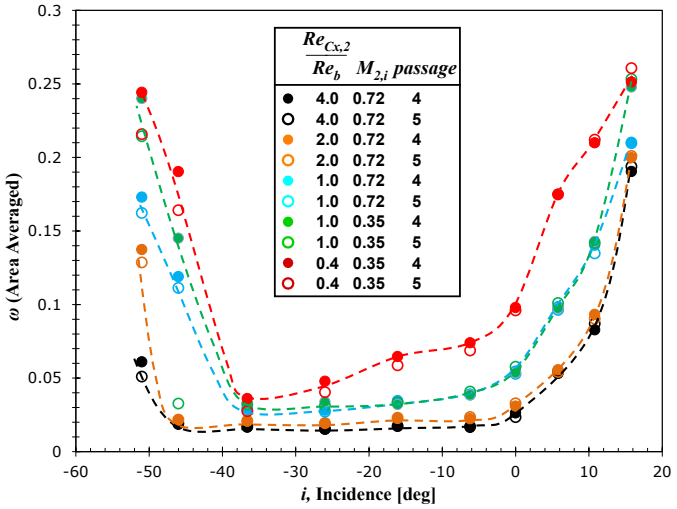

Figure 18.—Midspan Loss Versus Incidence.

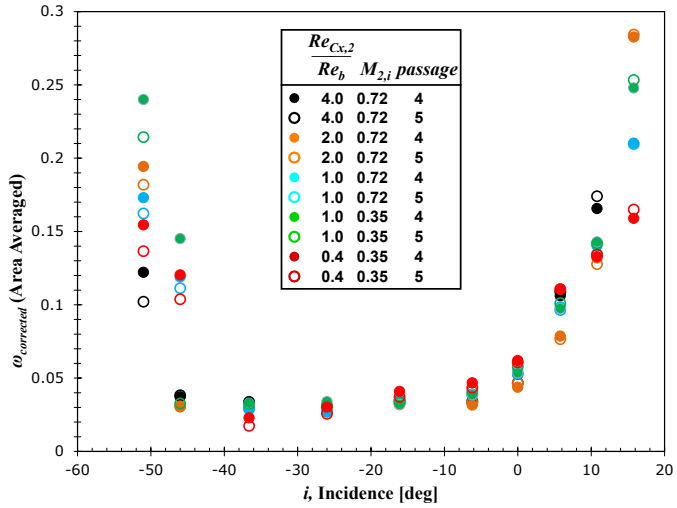

Figure 19.—$Re^{-0.5}$ Scaled Midspan Loss Versus Incidence.

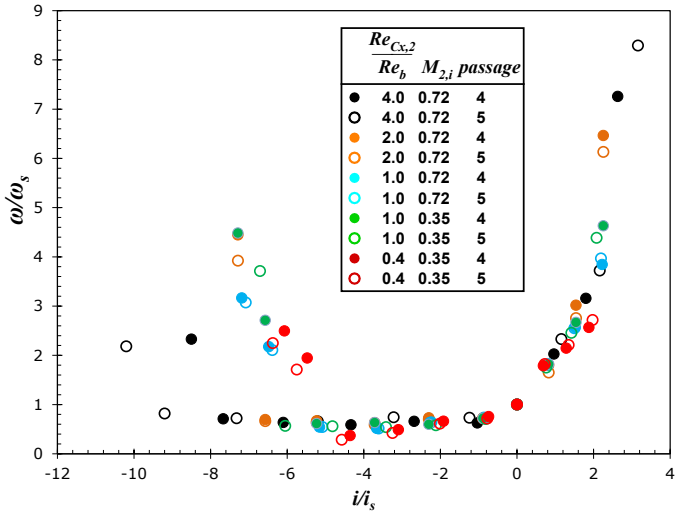

Figure 20.—Midspan Loss Bucket on Ainley-Mathieson Scaling.

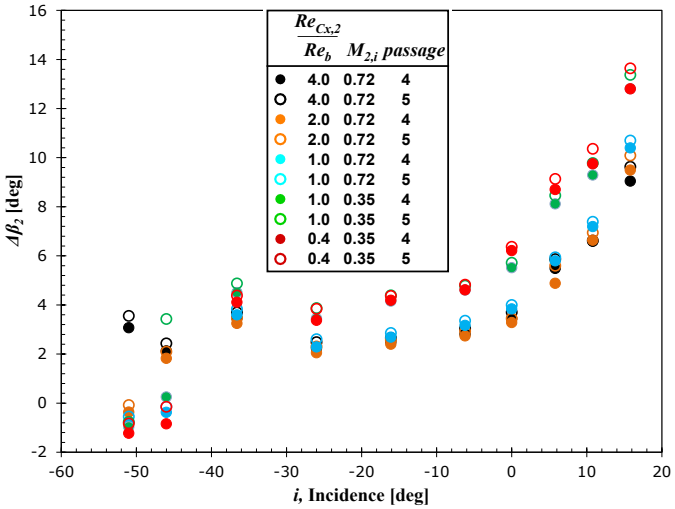

Figure 21.—Midspan Deviation Angle From Exit Metal Angle as Function of Incidence and Reynolds number.

Conclusions

The effects of large variations in incidence angle and Reynolds number on a 2-D VSPT blade section were examined in this paper. The exit total-pressure, flow angles, blade loading and endwall static pressures were documented.

Detailed survey data at the blade exit reflect transport of low momentum flow by strong secondary flows at the highly loaded positive incidence angles. The secondary flows decreased at the negative incidence angles as the blade row was unloaded and turning was reduced. The flow field was essentially two-dimensional at this unloaded condition.

Measured blade loadings reflected transitional flow on the suction surface. With the exception of the maximum Reynolds number condition, the loading diagrams were consistent with a laminar separation, transition, and subsequent reattachment as a turbulent boundary layer. Reverse loading reflected negative flow turning at the higher negative incidence angles. Separation was also noted on the pressure surface at extreme negative incidence angles.

Midspan loss levels decreased with increasing negative incidence until pressure-side cove separation occurred. Loss levels increased with decreasing Reynolds number as expected, and the range of incidence at acceptable loss levels decreased.

The midspan loss bucket collapsed strongly on a laminar power-law scaling ($\omega \propto Re^{-0.5}$). Also, rescaling the midspan loss versus incidence data according to the Ainley-Mathieson scaling illustrated a strong collapse, highlighting the need to accommodate Reynolds number changes on the incidence range of the canonical loss bucket.

The current tests were conducted at low turbulence inlet conditions. This dataset is planned to be augmented with data obtained on the same VSPT blade at higher inlet turbulence intensity in order to document the impact of turbulence intensity on the steady-state aerodynamic performance.

References

1. D′Angelo, M., “Wide Speed Range Turboshaft Study,” NASA CR-198380, Aug. 1995.
2. Welch, G.E., “Assessment of Aerodynamic Challenges of a Variable-Speed Power Turbine for Large Civil Tilt-Rotor Application,” Proc. AHS Int. 66th Annual Forum, May, 2010; also NASA/TM—2010-216758, Aug. 2010.
3. Johnson, W., Yamauchi, G. K., and Watts, M.E., “NASA Heavy Lift Rotorcraft Systems Investigation,” NASA/TP—2005-213467, Sep. 2005.
4. Acree, C.W., Hyeonsoo, Y., and Sinsay, J.D., “Performance Optimization of the NASA Large Civil Tiltrotor,” Proc. Int. Powered Lift Conf., London, UK, Jul. 22-24, 2008.
5. Snyder, C.A. and Thurman, D.R., Gas Turbine Characteristics for a Large Civil Tilt-Rotor (LCTR), Proc. AHS Int. 65th Ann. Forum, May 2009.
6. Hourmouziadis, J., “Aerodynamic Design of Low Pressure Turbines,” in Blading Design for Axial Turbomachines, AGARD-LS-167, pp. 8-1 to 8-40, 1989.
7. Haselbach, F., Schiffer, H.-P., Horsman, M., Dressen, S., Harvey, N., and Read, S., “The Application of Ultra High Lift Blading in the BR715 LP Turbine,” J. Turbomachinery, **124**, Jan. 2002, pp. 45-51.
8. Gier, J., Franke, M., Hübner, N. and Shröder, T., “Designing LP Turbines for Optimized Airfoil Lift,” ASME-GT2008-51101, 2008.
9. Halstead, D. E., Wisler, D. C., Okishii, T. H., Walker, G. J., Hodson, H.P, Shin, H-W., “Boundary Layer Development in Axial Compressors and Turbines: Part 3 of 4–LP Turbines,” J. Turbomachinery, **119 (2)**, pp. 225-237, April 1997.
10. Coull, J.D., Thomas, R.L., Hodson, H.P., 2010, “Velocity Distributions for Low Pressure Turbines,” J. Turbomachinery, **132**, Oct, pp. 041006-1 – 13.
11. Moustapha, S.H., Kacker, S.C., and Tremblay, B., 1990, “An improved incidence losses prediction method for turbine airfoils,” J. Turbomachinery, **112**, Apr., pp. 267-276.
12. Yamamoto, A. and Nouse, H., “Effects of Incidence on Three-Dimensional Flows in a Linear Turbine Cascade,” 1988, J. Turbomachinery, **110** (4), Oct., pp. 486 (11 pages).
13. Jouini, D.B.M., Sjolander, S.A., and Moustapha, S.H., 2002 “Midspan Flow-Field Measurements for Two Transonic Linear Turbine Cascades at Off-Design Conditions,” J. Turbomachinery, Apr., pp. 176-187. Vol. 124.
14. Hoheisel H., Kiock, R., Lichtfuss, H.J., and Fottner, L., 1987, “Influence of free-stream turbulence and blade pressure gradient on boundary layer and loss behavior of turbine cascades,” J. Turbomachinery, **109**, April, pp. 210-219.

15. Corriveau, D. and Sjolander, S. A., 2004, "Influence of Loading Distribution on the Performance of Transonic High Pressure Turbine Blades," J. Turbomachinery, Vol. **126**, Apr., pp.288-296.
16. Verhoff, V.G., Camperchioli, W.P, and Lopez, I., 1992, "Transonic Turbine Blade Cascade Testing Facility", AIAA Paper No. 92-4034, NASA TM-105646.
17. Giel, P.W., Sirbaugh, J.R, Lopez, I., and Van Fossen, G. J., 1996b, "Three Dimensional Navier Stokes Analysis and Redesign of an Imbedded Bellmouth Nozzle in a Turbine Cascade Inlet Section," ASME Journal of Turbomachinery, **118**, No. 3, pp. 529-535. NASA TM–107284 and U.S. Army ARL-MR-152.
18. McVetta, A.B., Giel, P.W., and Welch, G.E., "Aerodynamic Investigation of Incidence Angle Effects in a Large Scale Transonic Turbine Cascade," AIAA-2012-3879, Proc. 48th AIAA/ASME/SAE/ASEE Joint Propulsion Conference & Exhibit, Atlanta, GA, Jul.-Aug. 2012.
19. Giel, P.W., Thurman, D.R., Lopez, I., Boyle, R.J., Van Fossen, G.J., Jett T.A., Camperchioli, W.P., La, H., "Three Dimensional Flow Field Measurements in a Transonic Turbine Cascade," ASME 96-GT-113, 1996. Also NASA TM-107388 and U.S. Army ARL-TR-1252.
20. Giel, P.W., Bunker, R.S., VanFossen, G.J., and Boyle, R.J., 2000, "Heat Transfer Measurements and Predictions on a Power Generation Gas Turbine Blade," ASME 2000-GT-0209; Also NASA/TM—2000-210021.
21. Giel, P.W., Boyle, R.J., and Bunker, R.S., "Measurements and Predictions of Heat Transfer on Rotor Blades in a Transonic Turbine Cascade," J. Turbomachinery, **126** (1), pp. 110-121, Jan. 2004.
22. Coull, J.D., Thomas, R.L., Hodson, H.P., 2010, "Velocity Distributions for Low Pressure Turbines," J. Turbomachinery, **132**, Oct., pp. 041006-1 – 13.
23. Ford, A, Bloxham, M., Turner, E., Clemens, E. and Gegg, S., "Design Optimization of Incidence-Tolerant Blading Relevant to Large Civil Tilt-Rotor Power Turbine Applications," NASA/CR—2012-217016, Dec. 2012.
24. Smith, S.F., "A Simple Correlation of Turbine Efficiency," J. Royal Aero. Soc., **69**, 1965, pp. 467-470.
25. Brear, M.J., Hodson, H.P., and Harvey, N.W., "Pressure Surface Separations in Low-Pressure Turbines – Part I: Midspan Behavior," J. Turbomachinery, **124**, July, 2002, pp. 393-401.
26. Ainley, D.G. and Mathieson, G.C.R., "A Method of Performance Estimation for Axial-Flow Turbines," Aeronautical Research Council (ARC), R&M 2974, 1957.

REPORT DOCUMENTATION PAGE	Form Approved OMB No. 0704-0188

1. REPORT DATE *(DD-MM-YYYY)*	2. REPORT TYPE	3. DATES COVERED *(From - To)*
01-08-2013	Technical Memorandum	

4. TITLE AND SUBTITLE
Aerodynamic Measurements of a Variable-Speed Power-Turbine Blade Section in a Transonic Turbine Cascade at Low Inlet Turbulence

5a. CONTRACT NUMBER

5b. GRANT NUMBER

5c. PROGRAM ELEMENT NUMBER

6. AUTHOR(S)
Flegel-McVetta, Ashlie, B.; Giel, Paul, W.; Welch, Gerard, E.

5d. PROJECT NUMBER

5e. TASK NUMBER

5f. WORK UNIT NUMBER
WBS 877868.02.07.03.01.02.01

7. PERFORMING ORGANIZATION NAME(S) AND ADDRESS(ES)
National Aeronautics and Space Administration
John H. Glenn Research Center at Lewis Field
Cleveland, Ohio 44135-3191

8. PERFORMING ORGANIZATION REPORT NUMBER
E-18745

9. SPONSORING/MONITORING AGENCY NAME(S) AND ADDRESS(ES)
National Aeronautics and Space Administration
Washington, DC 20546-0001

10. SPONSORING/MONITOR'S ACRONYM(S)
NASA

11. SPONSORING/MONITORING REPORT NUMBER
NASA/TM-2013-218069

12. DISTRIBUTION/AVAILABILITY STATEMENT
Unclassified-Unlimited
Subject Categories: 07 and 34
Available electronically at http://www.sti.nasa.gov
This publication is available from the NASA Center for AeroSpace Information, 443-757-5802

13. SUPPLEMENTARY NOTES

14. ABSTRACT
Aerodynamic measurements obtained in a transonic linear cascade were used to assess the impact of large incidence angle and Reynolds number variations on the 3-D flow field and midspan loss and turning of a 2-D section of a variable-speed power-turbine (VSPT) rotor blade. Steady-state data were obtained for ten incidence angles ranging from +15.8° to −51.0°. At each angle, data were acquired at five flow conditions with the exit Reynolds number (based on axial chord) varying over an order-of-magnitude from 2.12×10^5 to 2.12×10^6. Data were obtained at the design exit Mach number of 0.72 and at a reduced exit Mach number of 0.35 as required to achieve the lowest Reynolds number. Midspan total-pressure and exit flow angle data were acquired using a five-hole pitch/yaw probe surveyed on a plane located 7.0 percent axial-chord downstream of the blade trailing edge plane. The survey spanned three blade passages. Additionally, three-dimensional half-span flow fields were examined with additional probe survey data acquired at 26 span locations for two key incidence angles of +5.8° and −36.7°. Survey data near the endwall were acquired with a three-hole boundary-layer probe. The data were integrated to determine average exit total-pressure and flow angle as functions of incidence and flow conditions. The data set also includes blade static pressures measured on four spanwise planes and endwall static pressures. Tests were conducted in the NASA Glenn Transonic Turbine Blade Cascade Facility. The measurements reflect strong secondary flows associated with the high aerodynamic loading levels at large positive incidence angles and an increase in loss levels with decreasing Reynolds number. The secondary flows decrease with negative incidence as the blade becomes unloaded. Transitional flow is admitted in this low inlet turbulence dataset, making it a challenging CFD test case. The dataset will be used to advance understanding of the aerodynamic challenges associated with maintaining efficient power turbine operation over a wide shaft-speed range.

15. SUBJECT TERMS
Turbines; Turbomachinery; Axial flow turbines; Tilt rotor craft; Aerodynamics

16. SECURITY CLASSIFICATION OF:			17. LIMITATION OF ABSTRACT	18. NUMBER OF PAGES	19a. NAME OF RESPONSIBLE PERSON
a. REPORT	b. ABSTRACT	c. THIS PAGE			STI Help Desk (email:help@sti.nasa.gov)
U	U	U	UU	22	19b. TELEPHONE NUMBER *(include area code)* 443-757-5802